Research Article

Reactive flash sintering of $SrFe_{12}O_{19}$ ceramic permanent magnets

A.F. Manchón-Gordón [a],*, P.E. Sánchez-Jiménez [a,b], J.S. Blázquez [c], A. Perejón [a,b], L.A. Pérez-Maqueda [a],*

[a] *Instituto de Ciencia de Materiales de Sevilla, ICMSE CSIC-Universidad de Sevilla, C. Américo Vespucio 49, Sevilla 41092, Spain*
[b] *Departamento de Química Inorgánica, Facultad de Química, Universidad de Sevilla, Sevilla 41012, Spain*
[c] *Dpto. Física de la Materia Condensada, ICMSE-CSIC, Universidad de Sevilla, P.O. Box 1065, 41080 Sevilla, Spain*

ARTICLE INFO

ABSTRACT

Reactive flash-sintering technique has been used in order to obtain strontium ferrite magnets from a mixture of $SrCO_3$ and Fe_2O_3 commercial powders. This technique allows preparing sintered $SrFe_{12}O_{19}$ at a furnace temperature of just 973 K during just 2 min by applying a modest field of 40 V cm^{-1}, instead of the conventional sintering process employed in ferrite magnet manufacturing that demands high temperature and long dwell times. Analysis of structural and magnetic properties were performed as a function of time in which the flash event was held. Mössbauer spectra show the existence of five different kinds of local environments, confirming the formation of strontium hexaferrite. The resulting samples exhibit comparable magnetic properties to the state-of-the-art ferrite magnets. In particular, produced samples reach a coercivity of 0.4 T and a specific saturation magnetization of 70 Am^2 kg^{-1}.

1. Introduction

Magnetic materials and, particularly, permanent magnets play a key role in many applications including motors, recording media or high frequency devices, such as millimeter wave absorbers and rotators [1–3]. On the quest to find alternatives to the rare-earth based permanent magnets, hexaferrites are one of the most important alternatives families, reaching an annual production of one million tons [4–7]. Among them, one of the most studied compounds is strontium hexaferrite, $SrFe_{12}O_{19}$, due to the competitive advantages it offers including availability, price and environmental friendliness during both mining and production [6]. This hexaferrite, with magnetoplumbite structure, exhibits superior chemical stability [8], outstanding magnetocrystalline anisotropy and relatively high Curie temperature [9].

The preparation technique used to produce $SrFe_{12}O_{19}$ plays a key role in determining the magnetic properties and structure of the final product. The conventional and earliest method to prepare this compound is by calcination and subsequent sintering of a mixture of oxides and carbonates in a furnace at 1573 K [10]. However, this method consumes extensive energy and time, and produces large particles, which decrease the hard magnetic behavior of the sample

[6]. For that reason, different chemical synthesis approaches have been considered to prepare nanostructured ferrites, such as sol-gel [11] and hydrothermal [12] followed by calcination at high temperatures or precipitation in molten salt at temperatures up to 1473 K [13]. These methods usually require the use of solvents and relatively long or complex preparation procedures. Moreover, mechanochemical synthesis has been also proposed for preparing this compound with high coercivity and magnetic saturation [14]. However, it requires of high milling times (> 5+ h) [14–16] that promote iron contamination from the milling media limiting the energy-saving and cost-reducing. In this sense, flash sintering, a relatively novel technique by which the application of electric field at moderate temperatures leads to the fast densification of most oxides within a few seconds [17], has attracted the interest of the scientific community. The main advantages of FS when is compared to conventional techniques are the significantly reduced processing times and temperatures, which allows for substantial energy saving [18] and, at the same time, results in reduced grain size and volatilization losses [19]. Moreover, it has been recently shown that it is possible to simultaneously induce the reaction and densification of compounds from a mixture of their precursors oxides powders in green state [20]. This new methodology has been denominated reaction (or reactive) flash sintering (RFS) and has been used to prepare different materials. The more novel attempts by RFS have been aimed towards preparation of a wide range of ceramic composites [21–23], oxide compounds [18,24] and recently, even high-entropy oxides [25–27].

---

* Corresponding authors.
E-mail addresses: afmanchon@us.es (A.F. Manchón-Gordón),
aperejon@us.es (A. Perejón), maqueda@cica.es (L.A. Pérez-Maqueda).

In this work, SrFe$_{12}$O$_{19}$ samples were successfully prepared by reactive flash sintering in just few minutes starting from a mixture of Fe$_2$O$_3$ and SrCO$_3$ powders. The partial and final products of the flash process have been studied by X-ray diffraction, scanning electron microscopy, Mössbauer spectroscopy and magnetometry. To the best of our knowledge, there are no reports on the preparation of SrFe$_{12}$O$_{19}$ or any other hard magnetic ceramic using RFS technique.

2. Experimental

Commercially available α-Fe$_2$O$_3$ (Sigma-Aldrich, ≥99 % purity) and SrCO$_3$ (Sigma-Aldrich, ≥98 % purity) were used for the preparation of the SrFe$_{12}$O$_{19}$ samples. The powders, with an additional amount of 5 % mass excess SrCO$_3$ [14,28,29], were mixed for 20 min with the objective of obtaining a homogeneous mixture in an Emax (Retsch) ball mill using hardened steel balls and vials as milling media. The initial powder mass was 10 g, the ball to powder ratio 10:1 and the speed of the vials of 500 rpm. To prevent the overheating of the vials, the experiments were carried out by alternating 5 min of milling with 1 min at rest.

Reaction flash sintering technique was employed in order to produce the SrFe$_{12}$O$_{19}$ compound. Approximately 0.8 g of the mixed precursors were uniaxially pressed into dog-bone shaped specimens and placed into a tubular furnace by means of two platinum wires attached to the handles of the dog-bone. Platinum paste was added into the holes of the handles of the green-body dog-bones in order to provide a good contact sample-electrode. The electrode wires were connected to a 1500 W DC power supply (EA-PSI 9760–06 DT). The furnace was heated from room temperature at a constant heating rate of 5 K/min and, simultaneously, the power supply was operated in a voltage-controlled mode until the flash event took place. As the sample conductivity increases, the current density traversing the specimen rises until a maximum preset value is reached. At this point, the power supply automatically switched to current-controlled mode to counteract the abrupt non-linear rise of the conductivity. The flash event was maintained for a certain time lag before the power supply was turned off.

Powder X-ray diffraction patterns, recorded in a Rigaku MiniFlex diffractometer using Cu-Kα radiation at room temperature, were used to monitor the formation of the strontium ferrite. The local environment of Fe atoms was analyzed at room temperature by Mössbauer spectrometry (MS) in transmission geometry using a ^{57}Co(Rh) source. Values of the hyperfine parameters were obtained by fitting the measured spectra with the NORMOS program [30] and

isomer shifts were measured relative to that of a standard foil of pure Fe at room temperature.

Microstructural analysis of the samples was carried out by scanning electron microscopy (SEM) in secondary electrons mode performed in a Hitachi S-4800 microscope (Hitachi, Ltd.) operated at 2 kV. Phase transition temperatures of the samples were determined by differential scanning calorimetry (DSC), and SrCO$_3$ decomposition was studied by thermogravimetric (TG) curves. These experiments were carried out in a simultaneous TG/DSC (Q650 SDT, TA Instruments), at a heating rate of 10 K/min under a nitrogen flow of 100 cm^3 min^{-1}.

Magnetic hysteresis loops for all the consolidated pellets were measured at room temperature under a maximum applied external magnetic field of ±1.5 T using a Lakeshore 7407 Vibrating Sample Magnetometer (VSM).

3. Results and discussion

3.1. Preparation of SrFe$_{12}$O$_{19}$ by reactive flash sintering

A careful control of the experimental conditions (applied electric field and current density limit) is essential to develop high quality samples by reactive flash sintering [31–33]. In this section, we have investigated reactive flash sintering, in which Fe$_2$O$_3$ and SrCO$_3$ can react and sinter and the same time to produce a single phase of a complex ferrite, SrFe$_{12}$O$_{19}$. In order to do that, up to 16 different experiments have been performed using different combinations of electric fields and current density limits. The obtained results are shown in Fig. 1. Well-differentiated regions can be observed: two large regions where reaction process was either incomplete (presence of precursor phases) or localized producing heterogeneous pellets (the localization of the current represents a preferential path for current flow through the specimen, which avoids the production of homogeneous samples with the desired microstructure [34]), and a very narrow range where the conditions in terms of applied electric fields and current density limits are optimum (complete formation of the desired structured without localization of the current) for the preparation of homogeneous materials. According to Fig. 1, at least an electric field of 40 V cm^{-1} and a current density limit of 80 mA mm^{-2} are needed to induce the reaction (blue symbols), while for lower values the reaction is incomplete. Therefore, optimum conditions are 40 V cm^{-1} and current density limits in the range from 80 to 100 mA mm^{-2}. Only under these specific conditions, homogeneous samples can be prepared without distortion of the current flow. In any other case, experimental conditions lead to localization (red symbols) or to incomplete reactions and poorly dense pellets (black symbols).

Fig. 2a shows, as an example, the evolution of electric field and current density as a function of the furnace temperature for a reactive flash sintering experiment at an electric field of 40 V cm^{-1}, a current density limit of 100 mA mm^{-2}, and with the flash event held for 0.5 min. The classical three stages of flash sintering [35] can be clearly observed. Incubation stage starts at approximately 913 K, where there is a slow increase in the conductivity of the sample. At stage II, there is a sharp rise in the conductivity to a maximum value of 100 mA mm^{-2}. At this point, the sample was maintained in a flash-activated state under controlled current for 0.5 min, which was reached at a furnace temperature of ~920 K.

Inset shows the power density dissipated during the reaction process in the specimen, given by $P = IE$, where I is the current density and E the electric field. The observed behavior at low temperatures is interrupted when the flash event occurs, with a sharp increase of the power dissipation. It is similar to those found in the literature for flash sintering of several materials but, in this case, reaction and sintering take place at the same time [36]. In fact, it has been shown that field-assisted processing techniques can enhance
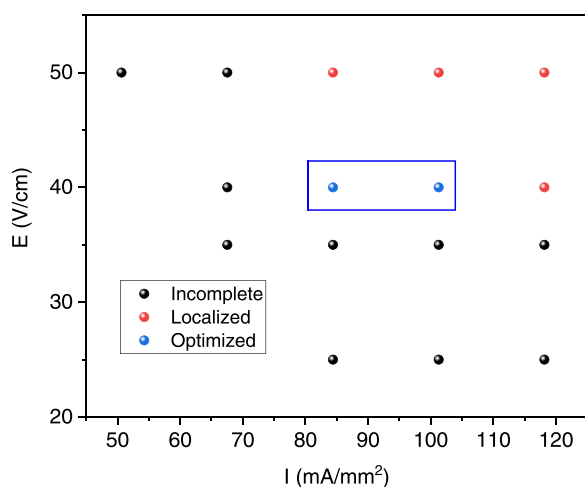

Fig. 1. Experimental conditions tested in the reactive flash sintering process of SrFe$_{12}$O$_{19}$, in terms of applied electric fields and current density limits (flash event holding 2 min).
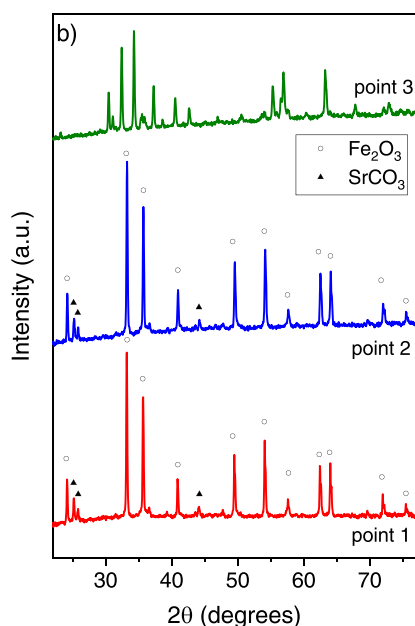
A.F. Manchón-Gordón, P.E. Sánchez-Jiménez, J.S. Blázquez et al.

Journal of Alloys and Compounds 922 (2022) 166203

Fig. 3. Thermogram corresponding to SrCO$_3$ decomposition.

points 1, and 2 and the flashed sample (point 3) is the formation of the hard magnetic SrFe$_{12}$O$_{19}$ (JCPDS 33-1340) after the flash event.

Thermogravimetric measurement for SrCO$_3$ initial powder is shown in Fig. 3. An important mass loss occurs between 1200 and 1400 K, due to the SrCO$_3$ decomposition into SrO and CO$_2$. These temperatures are much higher than those in which flash event is observed (Fig. 2a). In fact, it has been shown that the heat generated during the induction of the flash event of one of the constituents of the mixture can be used to induce the flash or other kinds of transformations, such as chemical reactions or decomposition, in the other compounds of the mixture [40]. Interestingly, in the studied samples, the flash event not only induces the formation of the ferrite, but it also induces the decomposition of the SrCO$_3$ at lower temperatures (point 3 in Fig. 2b). Therefore, strontium carbonate decomposition and chemical reaction to produce SrFe$_{12}$O$_{19}$ is concomitant to the flash process.

3.2. Structural characterization

Fig. 4a shows the XRD patterns taken at room temperature of the resulting pellets obtained after the flash experiment carried out under an electric field of 40 V cm^{-1}, a current limit of 100 mA mm^{-2} and with the flash event held for different times. Considering the XRD patterns, SrFe$_{12}$O$_{19}$ dominates the XRD reflections peaks, identified by hexagonal crystal lattice structure with $P6_3/mmc$ space group. Only in the case of sample flashed for 0.5 min, some traces of α-Fe$_2$O$_3$ phase can be observed (marked in the figure). This phase is identified by hexagonal crystal lattice structure with $R\bar{3}c$ space group and it is distinctly observed at the diffraction angle of 2θ~33 degrees. The appearance of α-Fe$_2$O$_3$ phase for the sample flashed for 0.5 min indicates the insufficient time and energy required for the formation of SrFe$_{12}$O$_{19}$ from α-Fe$_2$O$_3$ and SrCO$_3$. There is no evidence of α-Fe$_2$O$_3$ in XRD patterns collected when holding times of 2 min and 5 min are used.

A Le Bail fitting was performed to estimate the lattice parameters of the SrFe$_{12}$O$_{19}$ structure for the three studied specimens. Fig. 4b shows, as an example, the Le Bail refinement at room temperature of the XRD pattern corresponding to the sample flashed for 2 min. The obtained values of lattice parameters a and c as well as the crystal size, D, corresponding to the SrFe$_{12}$O$_{19}$ structure, have been collected in Table 1. These results show that the experimental X-ray profile fits well the calculated pattern with good confidence factors. The obtained values of the cell parameters are similar to those obtained for pure SrFe$_{12}$O$_{19}$ structure [41]. The worst GOF obtained in the case of the sample flashed for 0.5 is due to the existence of the residual α-Fe$_2$O$_3$ phase. On the other hand, an increase of D can be observed with the increase of time of flash, as it was expected for a higher exposition to high temperature of the samples.
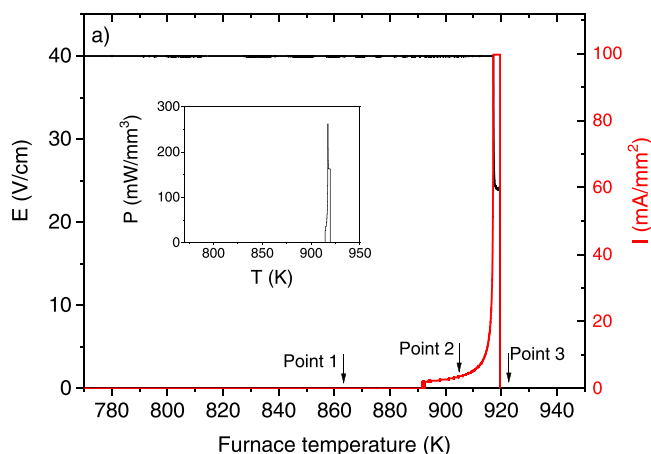

Fig. 2. a) Evolution of electric field and current density as a function of furnace temperature during a reactive flash experiment carried out at an electric field of 40 V cm^{-1}, a current density limit of 100 mA mm^{-2}, and a flash event held for 0.5 min. Arrows indicate the corresponding temperatures up to which different samples have been heated. Inset: power dissipation profile of the resulting pellet. b) X-ray diffraction patterns recorded at room temperature of the samples taken at the indicated points in a). All the peaks of the pattern at the point 3 correspond to SrFe$_{12}$O$_{19}$ (JCPDS 33-1340).

the kinetics of powder synthesis, accelerate sintering processes, and drive phase transformation at significantly lower temperatures compared to conventional methods [37]. Although it has been shown that synthesis and sintering of materials can be both remarkably accelerated by using electric fields, the reaction and densification could happen either simultaneously [20,38] or not [39].

Ex-situ XRD patterns (Fig. 2b) were taken at different temperatures during the reactive flash experiment (marked in Fig. 2a). At 863 K (point 1), the obtained XRD pattern is consistent with the mixture of the starting materials, where all the peaks correspond to Fe$_2$O$_3$ and SrCO$_3$. At 936 K, which corresponds to a furnace temperature at the beginning of the increase of the conductivity (point 2), the XRD pattern can be still indexed with the starting compounds. At this point we can conclude that these experimental conditions do not provide enough energy to produce the reaction corresponding to the formation of the strontium hexaferrite. The most crucial difference among the XRD patterns of the samples at
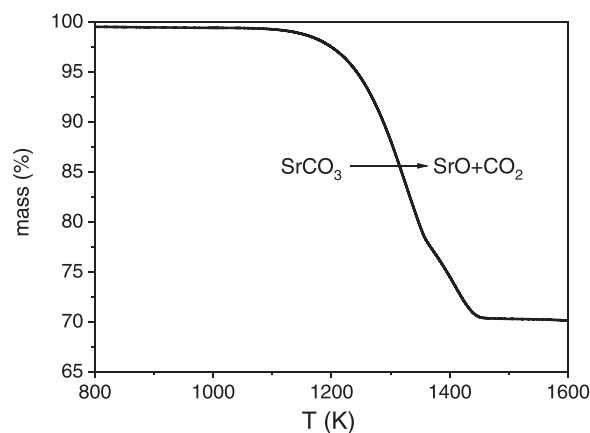
A.F. Manchón-Gordón, P.E. Sánchez-Jiménez, J.S. Blázquez et al.

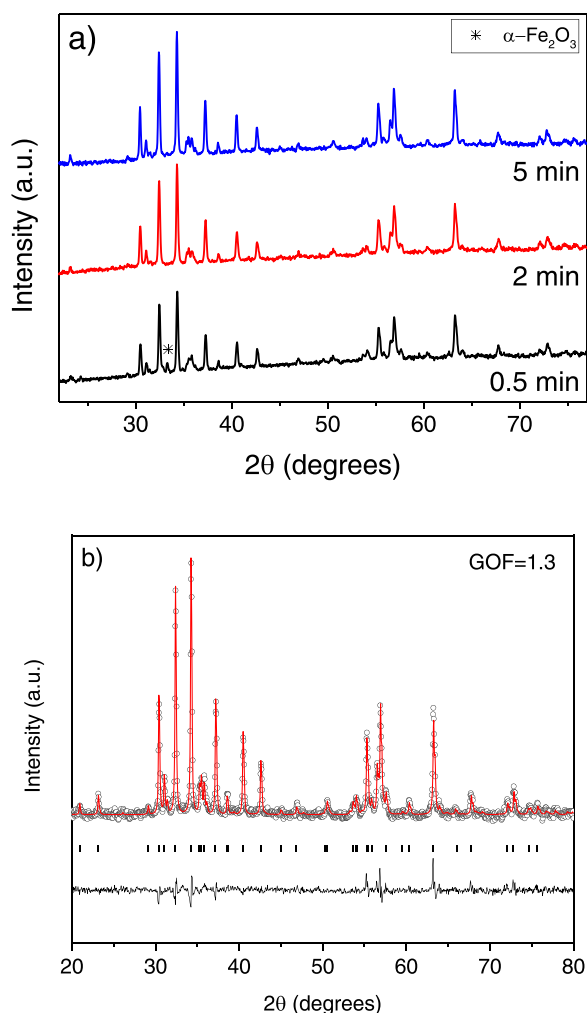Journal of Alloys and Compounds 922 (2022) 166203

Fig. 4. a) X-ray diffraction patterns at room temperature of the resulting pellets obtained after the reactive flash process carried out under an electric field of 40 V cm^{-1} and a current density limit of 100 mA mm^{-2} and held during different times. The main reflection peak of hematite (α-Fe_2O_3) is indicated in the figure. b) Le Bail refinement of the XRD pattern corresponding to the specimen reactive flashed for 2 min.

Table 1
Le Bail refinement parameters of the specimens flashed during different times at an electric field of 40 V cm^{-1} and a current density limit of 100 mA mm^{-2}.

Time (min)	a (Å)	c (Å)	D (nm)	GoF
0.5	5.870	23.000	62.0	1.8
2	5.872	23.015	63.5	1.3
5	5.875	23.030	77.2	1.5

^{57}Fe Mössbauer spectroscopy is a powerful tool for studying the local magnetic properties of materials which contains Fe [42,43]. This technique allows to obtain different information from their spectra. In this work, the use of this technique has allowed the quantitative analysis of the different phases which present the analyzed compounds, their identification and their magnetic characterization. Fig. 5 shows the room temperature Mössbauer spectra obtained from the prepared samples. One ferromagnetic site was used to describe the ferromagnetic contribution of the original mixed powder, assigned to single site in α-Fe_2O_3 phase. The spectra of the samples after the flash process show a complex behavior. In fact, the $SrFe_{12}O_{19}$ structure can be considered as a sequence of alternating spinel and rocksalt blocks, where the 24 iron cations are distributed over five different sub-lattices, with five different cation environments which correspond to the 2a, 2b, 4f1, 4f2, and 12k

positions in the Wickhoff notation [44]. At the spinel block, iron at the four octahedral (4f1) sites are antiferromagnetically coupled. In the rocksalt block, the presence of the Sr^{2+} distorts the neighboring octahedral iron sites, and gives rise to two distorted octahedral sites (4f2) which are antiferromagnetically coupled to the rest of the octahedral sites (12k). It also has an unusual bipyramidal Fe site (2b), coupled ferromagnetically to the majority of octahedral sites. Therefore, Mössbauer spectra have been fitted using five ferromagnetic sextets, one for each iron crystallographic site. Moreover, beyond the corresponding sextets of the $SrFe_{12}O_{19}$ structure, a distribution of hyperfine fields from 46 to 54 T was used to show the contribution of the α-Fe_2O_3 phase. Although a more realistic model should fit this contribution using only a discrete site, this procedure is generally found when analyzing disordered systems with complex unit cell in order to avoid overlapping and difficulties in the convergence of the fitting [42]. Even though the α-Fe_2O_3 phase was only detected by XRD in the case of the sample flashed for 0.5 min, the area fraction of this phase is evident by the Mössbauer spectra in the other specimens. In fact, it is known that MS is a more sensitive technique than XRD in order to detect small fractions of Fe compounds [42].

The hyperfine parameters obtained from the fit of the Mössbauer spectra are summarized in Table 2 for each of the five crystallographic sub-lattices. The obtained hyperfine parameters and spectral areas are all reasonably within the range of those reported previously for this material. The hyperfine field, as well as the quadrupolar splitting of the $SrFe_{12}O_{19}$ samples, show similar values to the previously obtained for this ferrite [45,46]. The isomer shift, δ, of all iron cations reaches values between 0.2 and 0.4 mm/s, indicating that iron exits in the 3 + state (typical value of δ for the 2 + state can be found in the range from 0.9 to 1.5 mm/s [46]). No significant variation in the different hyperfine field parameters can be found with the increase of the flash time.

The occupancy of the iron cations in the different sub-lattices are related with the area of each sub-spectrum normalized to 24 (last column of Table 2). It can be observed that the results of the sites 1–3 are somewhat higher than those theoretically expected (12, 4 and 2, respectively), obtaining lower values in the case of the sites 4 and 5 (corresponding to 4f2 and the 2b Wyckoff positions). These low values have been observed systematically in these kind of compounds [46,47], which have been associated to the presence of vacancies [47], which inhibit the exchange interactions and, therefore, decrease the magnetization. In fact, the presence of vacancies is habitual of this production route [48–51]. On the other hand, it should be noted that the best agreement between theoretical and experimental data is reached in the case of the sample flashed for 2 min, in which the amount of the Fe_2O_3 is lower.

The surface morphology of the cross section fracture of the reactive flash sintered specimen for 2 min, as observed by SEM, is shown in Fig. 6. The microstructure of the sample corresponds to a well-sintered material with a fairly uniform distribution of micrometric grains. The observed microstructure is typical of samples produced by RFS technique, characterized by reduced grain size [19]. In fact, the smaller grain sizes in RFSed samples were mainly attributed to the ultrafast densification under rapid heating. The density of the samples was estimated from Archimedes method, obtaining a relative density around 87 % using 5.1 g/cm^3 as the theoretical density value of $SrFe_{12}O_{19}$ [6].

3.3. Magnetic characterization

Fig. 7 shows the magnetic hysteresis loops $\sigma(H)$, where H is the applied field, recorded at 300 K for the studied specimens. The loops exhibit similar behavior, characterized by high coercive fields, H_C, as it is expected for hard magnets, and a considerable slope at high fields. It indicates that the saturation value of magnetization, σ_s,
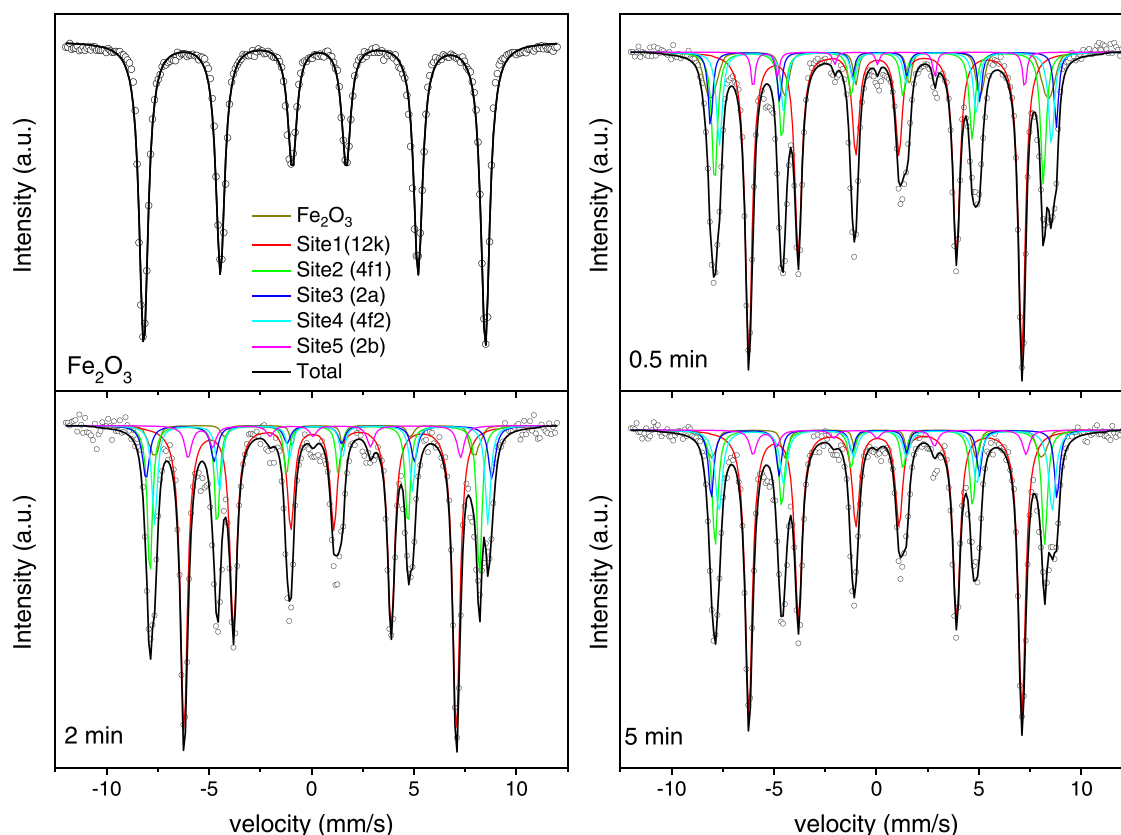
Fig. 5. Experimental (symbols) and fitting of the Mössbauer spectra (continuous lines) of the original mixed powders and of the resulting pellets obtained after the reactive flash process carried out under an electric field of 40 V cm^{-1}, a current density of 100 mA mm^{-2} and held during the indicated times.

could be only reached by means of higher applied fields. The specific magnetization at 1.5 T, $\sigma_{1.5T}$, and H_C have been collected in Table 3. The ferro-paramagnetic phase transition at the Curie temperature, T_C, has been observed from calorimetric measurements (Supplementary information). Obtained values of this parameter have been collected in Table 3, which are in close agreement with those of high quality samples reported in literature [9].

The obtained values of H_C are higher than those reported for samples produced by conventional solid-state reaction method [52], other techniques that require long dwell times and high

temperatures [53] and for SrFe$_{12}$O$_{19}$ nanocrystallites produced by hydrothermal synthesis and consolidated by Spark Plasma Sintering [29]. However, H_C values are lower than those found for samples produced by mechanochemical synthesis, but that require much more longer time of processing (5 h of milling + annealing at 973 K for 2 h) [14].

In order to estimate the value of σ_s, an approximation to saturation derived from the Stoner-Wohlfarth (SW) model has been used. In SW model, materials are considered as a single magnetic domain, so multi-domain related effects or inhomogeneities are not

Table 2
Hyperfine parameters obtained from the room temperature Mössbauer spectra of the analyzed samples. B_{hf} is the magnetic hyperfine field, Q_S is the quadrupolar splitting, δ the isomer shift relative to α-Fe and A the Fe atomic fraction of each contribution. Intensity corresponds to the occupancy of the iron cations in the sub-lattices of the SrFe$_{12}$O$_{19}$ structure normalized to 24. Estimated errors in B_{hf}, δ, Q, and A are $\pm$0.3 T, 0.03 mm/s 0.02 mm/s and 0.1 respectively.

| Time (min)	Component		B_{hf} (T)	Q (mm/s)	δ (mm/s)	A (%)	Intensity
0	Fe$_2$O$_3$	Site 1	51.7	0.23	0.37	100	
0.5	Fe$_2$O$_3$	distribution	51.0	0.23	0.33	10.6	
	SrFe$_{12}$O$_{19}$	Site1 (12k)	41.3	0.39	0.35	48.8	13.2
		Site2 (4f1)	49.7	0.10	0.19	16.9	4.4
		Site3 (2a)	52.3	0.17	0.36	7.8	2.1
		Site4 (4f2)	50.2	0.18	0.45	12.5	3.3
		Site5 (2b)	41.1	1.60	0.30	3.3	1.0
2	Fe$_2$O$_3$	distribution	48.6	0.24	0.32	4.5	
	SrFe$_{12}$O$_{19}$	Site1 (12k)	41.2	0.38	0.35	51.3	12.9
		Site2 (4f1)	49.8	0.09	0.21	16.7	4.1
		Site3 (2a)	52.3	0.23	0.35	8.4	2.1
		Site4 (4f2)	50.4	0.26	0.45	13.9	3.5
		Site5 (2b)	41.2	1.60	0.30	5.2	1.5
5	Fe$_2$O$_3$	distribution	50.0	0.24	0.28	5.7	
	SrFe$_{12}$O$_{19}$	Site1 (12k)	41.3	0.37	0.35	50.3	12.8
		Site2 (4f1)	49.8	0.07	0.21	16.9	4.3
		Site3 (2a)	52.3	0.19	0.37	8.7	2.2
		Site4 (4f2)	50.4	0.26	0.41	14.1	3.6
		Site5 (2b)	41.2	1.67	0.28	4.3	1.1
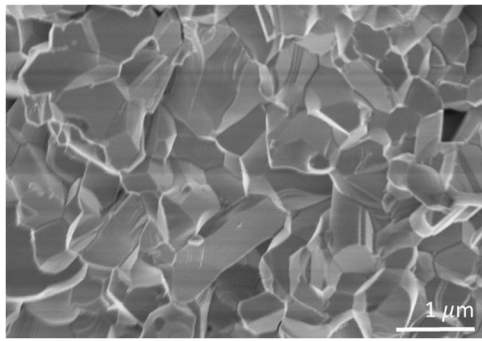
Fig. 6. SEM micrograph showing the microstructure of a cross section fracture of the SrFe$_{12}$O$_{19}$ sample prepared by reactive flash sintering at 40 V cm^{-1} and 100 mA mm^{-2} holding the flash event for 2 min.
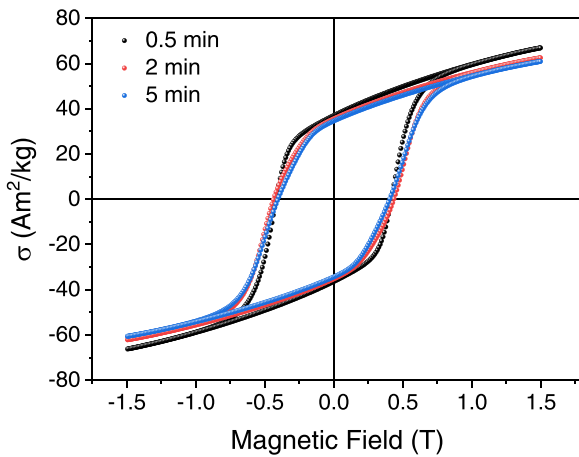

Fig. 7. Magnetic hysteresis loops taken at room temperature of the studied SrFe$_{12}$O$_{19}$ samples.

Table 3
Curie temperatures from the DSC experiments and magnetic parameters measured at room temperature of coercivity, H_C, remnant magnetization, σ_R, and magnetization at 1.5 T, $\sigma_{1.5}$, and the value of the saturation magnetization, σ_S. The values of the ratio σ_R/σ_S and the BH_{max} parameter have been included.

Time (min)	T_C (K)	H_C (T)	σ_R (Am^2 kg^{-1})	$\sigma_{1.5T}$ (Am^2 kg^{-1})	σ_S (Am^2 kg^{-1})	σ_R/σ_S (%)	BH_{max} (kJ/m^3)
0.5	734	0.43	36.6	66.9	74.2	0.49	30
2	734	0.42	35.4	62.5	68.9	0.51	24
5	734	0.40	34.5	60.9	67.3	0.51	21

considered. However, this simple model is adequate enough to describe the physics of magnetic grains that are small enough to contain single magnetic domains. Despite the simplicity of this model, it is capable to predict the existence of hysteresis loops for isotropic samples with identical particles. This approximation leads to the next equation [54]:

$$\sigma(H) = \sigma_s \ \ (1 - H_a^2\sin^2 2\theta_0/8H^2), \tag{1}$$

where H_a is the anisotropy field, and θ_0 is the angle between the applied field and the anisotropy axis. This model is intended for non-interacting, single domain particles with uniaxial anisotropy. From Eq. (1) it is expected a linear relationship of the measured magnetization at high fields as a function of $1/H^2$. This analysis has been applied to the studied specimens and depicted in Fig. 8, showing the expected linear behavior. The obtained σ_S, as expected, are higher than $\sigma_{1.5T}$ values and have been collected in Table 3.
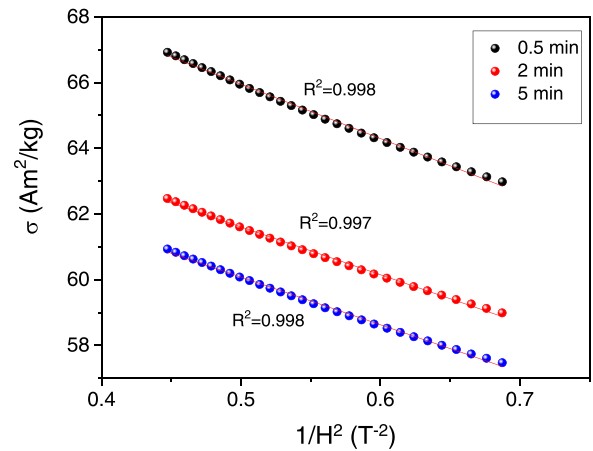

Fig. 8. Linear behavior of the magnetization at high field as a function of $1/H^2$ for the studied samples. R^2 is the correlation coefficient.

The ratio between remnant and saturation magnetization is commonly used in the evaluation of sample alignment. According to the SW model, an ideally aligned sample gives a ratio equal to unity, leading to hysteresis loops of enhanced rectangularity, while it decreases to 0.5 for complete randomly oriented crystallites [55]. The obtained ratio σ_R/σ_S of the studied samples is close to 0.5. Similar values of this ratio can be found in samples prepared by conventional methods [52]. However, clearly higher values have been reported when orientation methods are used in order to pre-align the powders during sintering [29,53,56]. σ_R/σ_S parameter is important to determine the energy product BH_{max}, which represents the energy stored outside the magnet in the magnetic field lines and is considered the figure of merit of a hard-magnetic material. For a fully dense and perfectly oriented sample with $\sigma_R=\sigma_S$, the theoretical upper limit of BH_{max} is given by $\mu_0\sigma_S^2/4$, where μ_0 is the vacuum permeability. For randomly oriented grains, where $\sigma_R=0.5\sigma_S$, a reduction in BH_{max} by a factor of 4 occurs. In the case of the studied samples, the theoretical maximum value of BH_{max} corresponds to 45 kJ/m^3 [2]. Our samples are far from this value, but they are similar to the highest BH_{max} value obtained for pre-aligned powders sintered by SPS (29(4) kJ/m^3) [29]. Moreover, this parameter has been determined without considering the demagnetizing factor. This fact implies that the obtained values for BH_{max} are just a minimum estimation of the parameter.

The differences found between the different studied specimens can be rationalized with the information provided by XRD and MS. A clear decrease of σ_S and H_C can be observed with the increase of the flash time, being the obtained values higher in the case of the sample flashed for 0.5 min H_C is directly related to the particle size and to optimize it, it is necessary to be in the narrow size range close to the critical diameter for single-domain particles, which for SrFe$_{12}$O$_{19}$ ranges from 0.6 to 1 μm [57]. In the studied samples, the impurities of α-Fe$_2$O$_3$ phase could act as an extra blockage of the magnetic wall movement. Moreover, Mössbauer spectra show a decrease of iron cations in 12k octahedral sites with the increase of the flash time, while the iron cations in tetrahedral positions are practically constant. It is known that the 12k octahedral sites point in the net magnetization direction of the SrFe$_{12}$O$_{19}$, while the 4 f tetrahedral cations point in the opposite direction. Therefore, the variation of the cation population detected by MS suggests a lower spin magnetic moment in the case of the samples flashed during longer time, in agreement with the obtained results. Moreover, although the effect of parameter a of the SrFe$_{12}$O$_{19}$ structure on the magnetic properties is not fully explained, it has been emphasized that the decrease in the parameter c causes an increase in magnetic

saturation [58], in agreement with the obtained results by XRD and magnetometry.

It is worth mentioning that using the reactive flash sintering technique, state-of-art nominal magnetic performance values are reached using a sintering process without dwell time, which implies an important reduction in the energy consumption required to produce ferrite magnets. This fact has been demonstrated for other ceramics produced by RFS, reaching a decrease of about 82 % in the energy consumption with respect to conventional preparation [18]. The obtained results indicate the good magnetic properties of the produced samples as well as point to enhance of the magnetic properties in RFS samples by applying an orientation method.

4. Conclusions

$SrFe_{12}O_{19}$ samples have been successfully synthesized and sintered in a single step by Reactive Flash Sintering technique, RFS, for the first time in just 2 min. Magnetic properties of the studied samples are closely linked to structural variations in the unit cells by the incorporation of the remnant hematite phase. Mössbauer analysis detects an increase of the occupation of tetrahedral sites with respect to octahedral ones when the flash time is increased, reflecting the reduction of the magnetic moments of the samples. The obtained values of coercivity, specific saturation magnetization and BH_{max} parameter can be compared with those previously reported and prepared by more complex techniques that require more time and energy. The results presented here show the potential of RFS technique for the synthesis and consolidation of $SrFe_{12}O_{19}$ magnets in a greener way, that leads to energy and time saving, which should translate well to other ceramic magnets.

CRediT authorship contribution statement

A.F. Manchón-Gordón: Conceptualization, Experiments, Formal analysis, Writing – original draft. **P.E. Sánchez-Jiménez:** Methodology, Supervision, Writing – review & editing, Resources. **J.S. Blázquez:** Conceptualization, Methodology, Supervision, Writing – review & editing, Resources. **A. Perejón:** Methodology, Supervision, Writing – review & editing, Resources. **L.A. Pérez-Maqueda**: Conceptualization, Resources, Methodology, Supervision, Writing – review & editing.

Data availability

Data will be made available on request.

Declaration of Competing Interest

The authors declare that they have no known competing financial interests or personal relationships that could have appeared to influence the work reported in this paper.

Acknowledgements

Appendix A. Supporting information

Supplementary data associated with this article can be found in the online version at doi:10.1016/j.jallcom.2022.166203.

References

[1] O. Gutfleisch, M.A. Willard, E. Brück, C.H. Chen, S.G. Sankar, J.P. Liu, Magnetic materials and devices for the 21st century: stronger, lighter, and more energy efficient, Adv. Mater. 23 (7) (2011) 821–842.

[2] J. Coey, Hard magnetic materials: a perspective, IEEE Trans. Magn. 47 (12) (2011) 4671–4681.

[3] R.W. McCallum, L.H. Lewis, R. Skomski, M.J. Kramer, I.E. Anderson, Practical aspects of modern and future permanent magnets, Annu. Rev. Mater. Res. 44 (1) (2014) 451–477.

[4] E.Y. Vedmedenko, R.K. Kawakami, D.D. Sheka, P. Gambardella, A. Kirilyuk, A. Hirohata, C. Binek, O. Chubykalo-Fesenko, S. Sanvito, B.J. Kirby, The 2020 magnetism roadmap, J. Phys. D Appl. Phys. 53 (45) (2020) 453001.

[5] C. Granados-Miralles, P. Jenuš, On the potential of hard ferrite ceramics for permanent magnet technology—a review on sintering strategies, J. Phys. D Appl. Phys. 54 (30) (2021) 303001.

[6] R.C. Pullar, Hexagonal ferrites: a review of the synthesis, properties and applications of hexaferrite ceramics, Prog. Mater. Sci. 57 (7) (2012) 1191–1334.

[7] M. Kimiabeigi, J.D. Widmer, R. Long, Y. Gao, J. Goss, R. Martin, T. Lisle, J.M.S. Vizan, A. Michaelides, B. Mecrow, High-performance low-cost electric motor for electric vehicles using ferrite magnets, IEEE Trans. Ind. Electron. 63 (1) (2016) 113–122.

[8] S. Rakshit, S. Parida, S. Dash, Z. Singh, R. Prasad, V. Venugopal, Thermochemical studies on SrFe12O19 (s), Mater. Res. Bull. 40 (2) (2005) 323–332.

[9] B.T. Shirk, W.R. Buessem, Temperature dependence of Ms and K1 of BaFe12O19 and SrFe12O19 single crystals, J. Appl. Phys. 40 (3) (1969) 1294–1296.

[10] D. Seifert, J. Töpfer, M. Stadelbauer, R. Grössinger, J.-M. Le Breton, Rare-earth-substituted Sr1−xLnxFe12O19 hexagonal ferrites, J. Am. Ceram. Soc. 94 (7) (2011) 2109–2118.

[11] T.T.V. Nga, N.P. Duong, T.T. Loan, T.D. Hien, Key step in the synthesis of ultrafine strontium ferrite powders (SrFe12O19) by sol–gel method, J. Alloy. Compd. 610 (2014) 630–634.

[12] A. Ataie, S. Heshmati-Manesh, Synthesis of ultra-fine particles of strontium hexaferrite by a modified co-precipitation method, J. Eur. Ceram. Soc. 21 (10) (2001) 1951–1955.

[13] S.-D. Kim, J.-S. Kim, Magnetic properties of Sr-ferrites synthesized in molten (NaCl+KCl) flux, J. Magn. Magn. Mater. 307 (2) (2006) 295–300.

[14] F. Sánchez-De Jesús, A.M. Bolarín-Miró, C.A. Cortés-Escobedo, R. Valenzuela, S. Ammar, Mechanosynthesis, crystal structure and magnetic characterization of M-type SrFe12O19, Ceram. Int. 40 (3) (2014) 4033–4038.

[15] K.M.U. Rehman, M. Riaz, X. Liu, M.W. Khan, Y. Yang, K.M. Batoo, S.F. Adil, M. Khan, Magnetic properties of Ce doped M-type strontium hexaferrites synthesized by ceramic route, J. Magn. Magn. Mater. 474 (2019) 83–89.

[16] İ. Kürşat, S. ÖZTÜRK, D.D. ÇAKIL, S.E. SÜNBÜL, Mechanochemical synthesis of SrFe12O19 from recycled mill scale: effect of synthesis time on phase formation and magnetic properties, J. Alloy. Compd. 873 (2021) 159787.

[17] M. Cologna, B. Rashkova, R. Raj, Flash sintering of nanograin zirconia in < 5 s at 850°C, J. Am. Ceram. Soc. 93 (11) (2010) 3556–3559.

[18] A. Taibi, S. Chaguetmi, P.E. Sánchez-Jiménez, A. Perejón, J.E. García, H. Satha, L.A. Pérez-Maqueda, Pure perovskite BiFeO3–BaTiO3 ceramics prepared by reaction flash sintering of Bi2O3–Fe2O3–BaTiO3 mixed powders, Ceram. Int. 47 (19) (2021) 26947–26954.

[19] L.A. Perez-Maqueda, E. Gil-Gonzalez, A. Perejon, J.M. Lebrun, P.E. Sanchez-Jimenez, R. Raj, Flash sintering of highly insulating nanostructured phase-pure BiFeO3, J. Am. Ceram. Soc. 100 (8) (2017) 3365–3369.

[20] E. Gil-González, A. Perejón, P.E. Sánchez-Jiménez, M.J. Sayagués, R. Raj, L.A. Pérez-Maqueda, Phase-pure BiFeO3 produced by reaction flash-sintering of Bi2O3 and Fe2O3, J. Mater. Chem. A 6 (13) (2018) 5356–5366.

[21] J.-C. M'Peko, Flash sintering in well-dispersed insulator-ionic conductor composites: the case of diphasic alumina-zirconia (Al2O3-3YSZ) system, Scr. Mater. 175 (2020) 38–42.

[22] Y. Jia, X. Su, Y. Wu, Z. Wang, L. Meng, X. Xu, A. Zhang, Flash sintering of 3YSZ/Al2O3–platelet composites, J. Am. Ceram. Soc. 103 (4) (2020) 2351–2361.

[23] P. Peng, Y. Deng, J. Niu, L. Shi, Y. Mei, S. Du, J. Liu, D. Xu, Fabrication and electrical characteristics of flash-sintered SiO2-doped ZnO-Bi2O3-MnO2 varistors, J. Adv. Ceram. 9 (6) (2020) 683–692.

[24] Y. Wu, X. Su, G. An, W. Hong, Dense Na0. 5K0. 5NbO3 ceramics produced by reactive flash sintering of NaNbO3-KNbO3 mixed powders, Scr. Mater. 174 (2020) 49–52.

[25] K. Wang, B. Ma, T. Li, C. Xie, Z. Sun, D. Liu, J. Liu, L. An, Fabrication of high-entropy perovskite oxide by reactive flash sintering, Ceram. Int. 46 (11) (2020) 18358–18361.

[26] H.-R. Mao, R.-F. Guo, R. Cao, S.-B. Jin, X.-M. Qiu, P. Shen, Ultrafast densification of high-entropy oxide (La0.2Nd0.2Sm0.2Eu0.2Gd0.2)2Zr2O7 by reactive flash sintering, J. Eur. Ceram. Soc. 41 (4) (2021) 2855–2860.

[27] H. Xiang, Y. Xing, Fz Dai, H. Wang, L. Su, L. Miao, G. Zhang, Y. Wang, X. Qi, L. Yao, H. Wang, B. Zhao, J. Li, Y. Zhou, , High-entropy ceramics: present status, challenges, and a look forward, J. Adv. Ceram. 10 (3) (2021) 385–441.

[28] E. Kiani, A.S. Rozatian, M.H. Yousefi, Synthesis and characterization of SrFe12O19 nanoparticles produced by a low-temperature solid-state reaction method, J. Mater. Sci. Mater. Electron. 24 (7) (2013) 2485–2492.

[29] M. Stingaciu, A.Z. Eikeland, F.H. Gjørup, S. Deledda, M. Christensen, Optimization of magnetic properties in fast consolidated SrFe12O19 nanocrystallites, RSC Adv. 9 (23) (2019) 12968–12976.

[30] R. Brand, J. Lauer, D. Herlach, The evaluation of hyperfine field distributions in overlapping and asymmetric Mossbauer spectra: a study of the amorphous alloy Pd77. 5-xCu6Si16. 5Fex, J. Phys. F Met. Phys. 13 (3) (1983) 675.

[31] E. Gil-González, A. Perejón, P.E. Sánchez-Jiménez, D. Román-González, L.A. Pérez-Maqueda, Control of experimental conditions in reaction flash-sintering of complex stoichiometry ceramics, Ceram. Int. 46 (18) (2020) 29413–29420.

[32] T.P. Mishra, C. Lenser, R. Raj, O. Guillon, M. Bram, Development of a processing map for safe flash sintering of gadolinium-doped ceria, J. Am. Ceram. Soc. 104 (9) (2021) 4316–4328.

[33] M. Biesuz, A. Ometto, V.M. Sglavo, Flash sintering of YSZ/Al2O3 composites: effect of processing and testing conditions, Materials 14 (4) (2021) 1031.

[34] G.M. Jones, M. Biesuz, W. Ji, S.F. John, C. Grimley, C. Manière, C.E. Dancer, Promoting microstructural homogeneity during flash sintering of ceramics through thermal management, MRS Bull. 46 (1) (2021) 59–66.

[35] J.S.C. Francis, R. Raj, Influence of the field and the current limit on flash sintering at isothermal furnace temperatures, J. Am. Ceram. Soc. 96 (9) (2013) 2754–2758.

[36] R. Raj, A. Kulkarni, J.-M. Lebrun, S. Jha, Flash sintering: a new frontier in defect physics and materials science, MRS Bull. 46 (1) (2021) 36–43.

[37] S.K. Jha, X.L. Phuah, J. Luo, C.P. Grigoropoulos, H. Wang, E. García, B. Reeja-Jayan, The effects of external fields in ceramic sintering, J. Am. Ceram. Soc. 102 (1) (2019) 5–31.

[38] B. Yoon, D. Yadav, S. Ghose, P. Sarin, R. Raj, On the synchronicity of flash sintering and phase transformation, J. Am. Ceram. Soc. 102 (6) (2019) 3110–3116.

[39] L.M. Jesus, R.S. Silva, J.-C. M'Peko, Ultrafast synthesis and sintering of materials in a single running experiment approach by using electric fields, J. Adv. Ceram. 8 (2) (2019) 265–277.

[40] L. Guan, J. Li, X. Song, J. Bao, T. Jiang, Graphite assisted flash sintering of Sm2O3 doped CeO2 ceramics at the onset temperature of 25 °C, Scr. Mater. 159 (2019) 72–75.

[41] X. Obradors, X. Solans, A. Collomb, D. Samaras, J. Rodriguez, M. Pernet, M. Font-Altaba, Crystal structure of strontium hexaferrite SrFe12O19, J. Solid State Chem. 72 (2) (1988) 218–224.

[42] A.F. Manchón-Gordón, J.J. Ipus, J.S. Blázquez, C.F. Conde, A. Conde, Evolution of Fe environments and phase composition during mechanical amorphization of Fe70Zr30 and Fe70Nb30 alloys, J. Non Cryst. Solids 494 (2018) 78–85.

[43] P. Gütlich, E. Bill, A.X. Trautwein, Mössbauer Spectroscopy and Transition Metal Chemistry: Fundamentals and Applications, Springer Science & Business Media, 2010.

[44] A. Morel, J.M. Le Breton, J. Kreisel, G. Wiesinger, F. Kools, P. Tenaud, Sublattice occupation in Sr1−xLaxFe12−xCoxO19 hexagonal ferrite analyzed by Mössbauer

[45] spectrometry and Raman spectroscopy, J. Magn. Magn. Mater. 242- 245 (2002) 1405–1407.

[45] M.D. Dyar, A review of Mössbauer data on inorganic glasses: the effects of composition on iron valency and coordination, Am. Mineral. 70 (3–4) (1985) 304–316.

[46] I.A. Auwal, A. Baykal, H. Güngüneş, S.E. Shirsath, Structural investigation and hyperfine interactions of BaBixLaxFe12−2xO19 (0.0≤x≤0.5) hexaferrites, Ceram. Int. 42 (2, Part B) (2016) 3380–3387.

[47] V. Sankaranarayanan, Q. Pankhurst, D. Dickson, C. Johnson, An investigation of particle size effects in ultrafine barium ferrite, J. Magn. Magn. Mater. 125 (1–2) (1993) 199–208.

[48] A. Karakuscu, M. Cologna, D. Yarotski, J. Won, J.S. Francis, R. Raj, B.P. Uberuaga, Defect structure of flash-sintered strontium titanate, J. Am. Ceram. Soc. 95 (8) (2012) 2531–2536.

[49] R. Zhao, D. Han, S. Lu, B. Song, M. Li, B. Fan, H. Wang, H. Xu, H. Lu, G. Shao, R. Zhang, Position–sensitive electric property of flash–sintered 3Y–TZP ceramics based on DC bias assisted impedance analysis, Ceram. Int. 48 (2) (2022) 2882–2885.

[50] S.E. Murray, G. Lv, S.S. Sulekar, D.G. Cahill, D.P. Shoemaker, In situ defect quantification and phase identification during flash sintering using Raman spectroscopy, J. Am. Ceram. Soc. 104 (8) (2021) 3873–3882.

[51] W. Xu, A. Maksymenko, S. Hasan, J.J. Meléndez, E. Olevsky, Effect of external electric field on diffusivity and flash sintering of 8YSZ: a molecular dynamics study, Acta Mater. 206 (2021) 116596.

[52] T. Pérez-Juache, A. Guerrero, J. Cabal-Velarde, M. Mirabal-García, S. Palomares-Sánchez, J. Matutes-Aquino, Analysis of the structure and Mössbauer study of the neodymium substitution in the Sr-hexaferrite, Phys. B Condens. Matter 503 (2016) 183–188.

[53] J.C. Guzmán-Mínguez, V. Fuertes, C. Granados-Miralles, J.F. Fernández, A. Quesada, Greener processing of SrFe12O19 ceramic permanent magnets by two-step sintering, Ceram. Int. 47 (22) (2021) 31765–31771.

[54] C. Tannous, J. Gieraltowski, The Stoner–Wohlfarth model of ferromagnetism, Eur. J. Phys. 29 (3) (2008) 475.

[55] E.C. Stoner, E. Wohlfarth, A mechanism of magnetic hysteresis in heterogeneous alloys, Philos. Trans. R. Soc. Lond. Ser. A Math. Phys. Sci. 240 (826) (1948) 599–642.

[56] A. Volodchenkov, S. Ramirez, R. Samnakay, R. Salgado, Y. Kodera, A. Balandin, J. Garay, Magnetic and thermal transport properties of SrFe12O19 permanent magnets with anisotropic grain structure, Mater. Des. 125 (2017) 62–68.

[57] J. Park, Y.-K. Hong, W. Lee, S.-Y. An, J.-W. Seo, K.-H. Hur, Coercivity of SrFe12O19 hexaferrite platelets near single domain size, IEEE Magn. Lett. 6 (2015) 1–3.

[58] F. Tenorio-González, A. Bolarín-Miró, F. Sánchez-De Jesús, P. Vera-Serna, N. Menéndez-González, J. Sánchez-Marcos, Crystal structure and magnetic properties of high Mn-doped strontium hexaferrite, J. Alloy. Compd. 695 (2017) 2083–2090.